Neutron densities and the single particle structure of several even-even nuclei from ^{40}Ca to ^{208}Pb

L. Ray
Theoretical Division, Los Alamos Scientific Laboratory, Los Alamos, New Mexico 87545

P. E. Hodgson
Nuclear Physics Laboratory, University of Oxford, Keble Road, Oxford OX1 3RH, United Kingdom
(Received 6 August 1979)

Previously developed techniques which sum the squares of proton single particle wave functions to obtain nuclear charge densities are applied to the study of neutron distributions in ^{40,48}Ca, ^{58,64}Ni, ^{116,124}Sn, and ^{208}Pb by comparing to those neutron densities deduced from 800 MeV proton elastic scattering data. The proton and neutron single particle wave functions are derived from a one-body, nonlocal Woods-Saxon binding potential whose parameters are adjusted to give the experimental single particle energies. Empirical spectroscopic factors determine the appropriate occupation probabilities for the single particle levels near the Fermi surface. Proper attention is given to nonorthogonality problems and to the removal of the spurious center-of-mass motion. These semiphenomenological neutron densities are compared to the predictions of the density matrix expansion variant of Hartree-Fock theory and to densities which are empirically deduced from recent 800 MeV polarized proton elastic scattering data. These "experimental" neutron distributions are obtained from approximate second order Kerman, McManus, and Thaler optical potential analyses using essentially "model independent" neutron densities. Qualitatively good agreement is obtained between the semiphenomenological neutron densities computed here, the density matrix expansion predictions, and the empirical results.

[NUCLEAR STRUCTURE Sums of squares of single particle wave functions; nonlocal potentials; nonorthogonality effects; computed proton and neutron one-body densities for ^{40,48}Ca, ^{58,64}Ni, ^{116,124}Sn, and ^{208}Pb.]

I. INTRODUCTION

The calculation of nuclear densities from various theoretical models comprises a significant fraction of the recent efforts expended in nuclear physics. Mean field theories,[1-3] shell-model approaches,[4,5] and Brueckner-Hartree-Fock techniques[6] typify these efforts. In addition to these methods, recent calculations of nuclear charge densities have been presented[7,8] which utilize empirical, single particle binding energies and spectroscopic strengths as determined from studies of single nucleon (mainly proton) transfer reactions. These calculations generate the nuclear charge densities by summing the squares of the moduli of nonlocal Woods-Saxon wave functions with proper care being given to nonorthogonality corrections,[7] center-of-mass motion,[1,2] proton and neutron electromagnetic form factors,[9] spin-orbit corrections,[9] and relativistic effects.[9] Although using explicit Woods-Saxon binding potential models, this technique has been able to obtain high quality reproduction of the "model independent" charge densities determined by electron scattering and muonic atom data for several nuclei.[7,8] Predicted nuclear charge densities, using average binding potentials,[10] are in very good agreement with several empirical densities from ^{16}O to ^{208}Pb.[10] Precision fits to empirical charge distributions can readily be obtained by a minor adjustment of parameters.[7,8] Thus, the utility of this model is that it permits one to relate, in a phenomenological sense, the copius amount of information gained from single nucleon transfer reactions to the equally abundant electron scattering and muonic atom data. By carrying out such studies as are presented in Refs. 7 and 8 one obtains a nuclear structure model for a particular nucleus which is consistent with the available nuclear reaction, electron scattering, and muonic atom data, at least with respect to the nuclear charge density.

In addition to the continued study of nuclear charge densities by this method, one should also test the accompanying neutron densities against empirical results. Thus, in this work we shall explore the feasibility of relating the volume of single neutron transfer reaction data to the empirically deduced neutron density distributions in nuclei by an application of this semiphenomenological model similar to that given in Refs. 7 and 8. Since empirical neutron densities in nuclei have not been obtained with as high a degree of reliability as have nuclear charge densities, our purpose here will be to make qualitative compari-

sons with these neutron distributions rather than attempting detailed fits as were done for the charge densities in Refs. 7 and 8. Thus, qualitative comparisons as given in Ref. 10 for the nuclear charge densities will be presented here for the neutron distributions in ^{40,48}Ca, ^{58,64}Ni, ^{116,124}Sn, and ^{208}Pb.

Considerable experimental and theoretical efforts have been expended in the last few years in an effort to gain empirical information about neutron densities in nuclei. Since strongly interacting probes such as the proton, alpha particle, or pion are often used in these investigations, the analyses of the scattering data are to varying degrees model dependent, and the results are always susceptable to theoretical uncertainties in the approximations to the many body scattering theories which must be invoked or to errors in the experimental hadronic scattering data which are analyzed.

Encouraging results have, however, recently been obtained by Glauber[11] and Kerman, McManus, and Thaler (KMT)[12] analyses of intermediate energy (~1 GeV) proton elastic scattering data. Experimentally, recent polarized proton elastic scattering data at 0.8 GeV obtained with the high resolution spectrometer (HRS) at the Clinton P. Anderson Meson Physics Facility (LAMPF) of the Los Alamos Scientific Laboratory have been of superb statistical quality.[13-16] Great care has been devoted to the precise determination of the absolute scattering angle and the overall normalization of the data.[16] These data together with the earlier 1 GeV unpolarized proton scattering results from Saclay[17,18] and Gatchina[19] have permitted studies of neutron distributions to be carried out in many nuclei ranging from ^{12}C to ^{208}Pb.[18,20,21] Many theoretical and numerical efforts have been performed which carefully investigate the importance of spin dependence,[14,20-22] target nucleon correlation corrections,[20,21,23,24] electromagnetic and relativistic corrections,[9,20] various improvements to the usual "impulse approximation,"[25] and the degree to which model dependence is important in the analysis.[22,26] Studies have also been made of the various sources of theoretical and experimental uncertainties which contribute to the total error in the deduced neutron densities obtained from these Glauber or KMT analyses.[22] The results of these experimental and theoretical efforts are deduced neutron density distributions and rms radii which are generally in favorable agreement with Hartree-Fock[1-3] and the density matrix expansion (DME)[2] predictions. Furthermore, the deduced densities obtained from Glauber and KMT analyses of the 0.8 and 1.0 GeV proton data are all in good agreement with each other in most cases.[13,22] Absolute tests of the accuracy of the approximate multiple scattering formulation as applied in these analyses are somewhat lacking, however. Energy dependent calculations of the total and total reaction cross sections using the second order KMT optical potential[27] have demonstrated that no gross, lowest order problems exist with this analytical method for proton energies greater than 400 MeV. This, together with the good agreement obtained between the deduced neutron densities and Hartree-Fock predictions suggest that these empirically deduced densities can be usefully compared to the results of the semiphenomenological method of Refs. 7 and 8.

In Sec. II a brief outline of the semiphenomenological technique of Refs. 7 and 8 for generating proton and neutron densities will be given as well as specifying the one nucleon transfer information used in the calculations for the nuclei considered here. The computed neutron densities for ^{40,48}Ca, ^{58,64}Ni, ^{116,124}Sn, and ^{208}Pb will also be compared to the predictions of the density matrix expansion (DME)[2,28] code of Negele in this section. In Sec. III a brief summary of the second order KMT optical potential method for computing proton-nucleus elastic scattering will be given. In Sec. IV the elastic cross sections and the radial density distributions and moments resulting from the calculations of Sec. II will be compared to the experimental data and the empirically deduced densities. General trends, significant agreements, and some notable disagreements between these various density models will be discussed. Relative isotopic neutron density differences will be studied here also. Finally in Sec. V a summary and some conclusions will be offered.

II. SEMIPHENOMENOLOGICAL COMPUTATION OF THE ONE-BODY DENSITIES

The method of generating nuclear densities by summing the squares of single particle wave functions has been described in detail in Ref. 7 and so will only be summarized here. The calculation begins by evaluating the single particle eigenstates of the Woods-Saxon potential

$$V(r) = -V_L f_1(r) + V_S(\hbar/m_\pi c)^2 \frac{1}{r}\frac{d}{dr} f_2(r)\vec{L}\cdot\vec{\sigma} + V_C(r), \tag{1}$$

where (for proton states only) $V_C(r)$ is the Coulomb potential corresponding to a uniform sphere of charge of radius $1.1A^{1/3}$ fm and

$$f_{1,2}(r) = \{1+\exp[(r-R_{1,2})/a_{1,2}]\}^{-1}, \tag{2}$$

with $R_2 = 1.1A^{1/3}$, $a_2 = 0.65$ fm, $R_1 = R_p$ or R_n, and $a_1 = a_p$ or a_n for protons or neutrons. The well

depth V_L is adjusted to reproduce the empirical single particle energies given by[7,8] (for both protons and neutrons)

$$E=\sum_{i=1}^{3}E_{Bi}S_i\Big/\sum_{i=1}^{3}S_i\,, \tag{3}$$

where E_{Bi} and S_i are the average binding energies and the summed spectroscopic factors obtained from one nucleon transfer reactions. The spin-orbit potential strength is adjusted to reproduce the spin-orbit splitting if known and is assumed to be 7 MeV otherwise. The single particle eigenstates of the potential in Eq. (1) which have the same $\{lJM\}$ quantum numbers but correspond to different well depths, V_L, are nonorthogonal. Nonlocality corrections, introduced to minimize this nonorthogonality, are parametrized by the nonlocality length β and have been included either by the method of Perey[29] or by the very similar prescription of Fiedeldey.[30] The resulting nonlocal single particle wave functions are still nonorthogonal. Following the Gram-Schmidt procedure[7] these nonorthogonal wave functions are expanded in an orthonormal basis $\{\phi_\alpha\}$. The occupation numbers of the nonorthogonal states, denoted by $\langle\bar{n}_\alpha\rangle$, are assumed to be equal to 1 for the deep levels[7,8] and are taken to be $\{(2J+1)^{-1}\langle\pi\rangle\}$ (or $\{(2J+1)^{-1}\langle\nu\rangle\}$), where $\langle\pi\rangle$ ($\langle\nu\rangle$) are the proton (neutron) shell occupation numbers obtained from spectroscopic factors in the case of the higher levels near the Fermi surface. By making special assumptions about the occupation numbers[7] one obtains a simple expression for the one-body nuclear density. This expression is[7]

$$\rho(r)=\sum_\alpha\langle n_\alpha\rangle\int dr'\,|y_\alpha(r')|^2 g(r,r')/r'^2\,, \tag{4}$$

where $\langle n_\alpha\rangle$ and $y_\alpha(r)$ are the occupation numbers and radial parts of the orthonormal basis functions, $\{\phi_\alpha\}$, and $g(r,r')$ is given by

$$g(r,r')=(4\pi)^{-1}\int d\Omega h(|\vec{r}-\vec{r}'|^2)\,, \tag{5}$$

where

$$h(x^2)=\sum_k d_k\pi^{-3/2}a_k^{-3}\exp(-x^2/a_k^2)\,, \tag{6}$$

which accounts for the finite nucleon size.[7] For point density distributions, $g(r,r')$ is proportional to $\delta(r-r')$. The above expressions are valid for spherically symmetric densities only. The sum in Eq. (4) includes all single particle orbitals which have a nonzero occupation probability. The simple expression for the density in Eq. (4) depends crucially on the assumptions about the single particle occupation numbers discussed in Ref. 7. The success of Eqs. (1)–(6) in reproducing "model independent" charge densities is well documented.[7,8] Equations (1)–(6) are similarly but separately used in the calculation of the proton and neutron densities.

The numerical details necessary in computing the nuclear charge densities are discussed in Refs. 7 and 8. The parameters which can be varied to fit the empirical charge densities are (1) the proton binding potential radius R_p, (2) the potential surface diffuseness a_p, (3) the nonlocality parameter β_p, (4) the binding energies of the deep lying proton single particle levels, and (5) the occupation numbers of the highest proton orbitals near the Fermi surface. The range of variation of these last two quantities is limited by experimental data. The parameters which most affect the computed charge density are the potential radius and diffuseness and the occupation numbers of the highest single particle levels. By varying these parameters the "model independent" charge densities of ^{40,48}Ca, ^{58}Ni, and ^{208}Pb[31-33] were fit as discussed in Refs. 7 and 8. Owing to the lack of availability of "model independent" charge densities for ^{64}Ni, ^{116}Sn, and ^{124}Sn, the theoretical charge densities for these nuclei were computed by assuming average parameters taken from nearby nuclei (from ^{58}Ni in the case of ^{64}Ni) and the results from systematic studies of the variation of the best fit parameters through the periodic table.[10] The empirical rms charge radii for these nuclei[34] were fit by adjusting parameters. The nuclear charge densities were computed by taking into account the finite proton and neutron charge distributions, the relativistic Darwin-Foldy term[9] and the center-of-mass correction[1,2] using Eq. (6) and the parameters given in Table I. Corrections for the spin-orbit contribution[9] to the nuclear charge density arising from the magnetic moment of the nucleon

TABLE I. Proton and neutron charge distribution parameters. The parameters of Eq. (6) (see text) used to evaluate the nuclear charge density. For protons, $d_{1,2,3}=0.506$, 0.328, 0.166, respectively. For neutrons, d_1, d_2, a_1, and a_2 equal 1.0, −1.0, 0.685, and 0.739 fm, respectively. The values of $a_{1,2,3}$ vary with mass owing to the center-of-mass correction (see Ref. 7).

Nucleus	a_1 (fm)	a_2 (fm)	a_3 (fm)
^{40}Ca	0.593	0.244	1.203
^{48}Ca	0.609	0.279	1.210
^{58}Ni	0.618	0.299	1.215
^{64}Ni	0.618	0.299	1.215
^{116}Sn	0.657	0.374	1.235
^{124}Sn	0.657	0.374	1.235
^{208}Pb	0.657	0.374	1.235

were also included. The spurious center-of-mass motion[1,2] was removed from all of the computed densities by the harmonic oscillator prescription[1,2] with the oscillator length parameters being fixed to yield the experimental rms radii.

A similar procedure has been followed in computing the neutron density distributions. In all the calculations presented here the neutron potential diffuseness and the neutron nonlocality parameter are assumed to be equal to those of the protons. The single particle binding energies and occupation numbers are determined by the average of the available experimental results.[10,35-59] Thus the only parameter which has been allowed to vary in these neutron density calculations is the neutron binding potential radius, R_n, which has been adjusted for each nucleus to yield two values of $\Delta r_{np} \equiv \langle r_n^2 \rangle^{1/2} - \langle r_p^2 \rangle^{1/2}$ which span the corresponding range of values given by Hartree-Fock[1-3] and DME[2,28] predictions and analyses of proton-nucleus elastic scattering near 1 GeV.[13-22]

The pertinent single particle energies, spectroscopic information and the local binding potential well depths, V_L, are given in Tables II–VIII for ^{40,48}Ca, ^{58,64}Ni, ^{116,124}Sn, and ^{208}Pb, respectively, for both protons and neutrons. The references which provide these experimental quantities are also given in each table.

In Fig. 1 the sensitivity of Δr_{np} for ^{48}Ca to the neutron potential diffuseness, nonlocality, binding energies, and the $2p_{3/2}$ occupation number is displayed. As can be seen in this figure, reasonable variations in any of these parameters produce less than 0.1 fm change in Δr_{np} which is comparable to the magnitude of the uncertainty in the theoretical[1-6] and "experimental" values.[13-22] Thus, the principal parameter affecting the computed neutron densities is the binding potential radius, R_n, and therefore for now will be the only parameter which is adjusted to yield comparisons with the empirical densities.

It is of considerable interest to compare the neutron densities computed by this semiphenomenological method to the predictions of the density matrix expansion code of Negele[2,28] with respect to the reproduction of interior quantum fluctuations and general surface and tail geometries. These comparisons are presented in Figs. 2–8 for ^{40,48}Ca, ^{58,64}Ni, ^{116,124}Sn, and ^{208}Pb, respectively. The DME predictions are indicated by the solid curves, while the neutron densities computed here are shown by the dashed (for the smaller values of Δr_{np}) and the dash-dot curves (for the larger Δr_{np}). The densities shown correspond to point neutron density distributions. Note that each density has been increased by a factor of 10 in the tail region for clarity. With the exception of ^{124}Sn, the densities computed here reproduce the general shapes and bracket the DME predictions. The DME calculation for ^{124}Sn assumes that the $3s_{1/2}$ single particle level is completely filled, whereas in the present calculation, this level is presumed to be empty. This difference in the assumed population of the $3s_{1/2}$ single particle level fully accounts for the qualitative difference between the density fluctuations in the nuclear interior of these two calculations. DME predictions which assume no $3s_{1/2}$ occupation qualitatively reproduce the dashed and dash-dot curves in Fig. 7 to the same degree as that displayed in Fig. 6 for ^{116}Sn. From Figs. 2–8 one can also see that, in general, the surface thickness of the semiphenomenological neutron densities are slightly smaller than those of the DME method. Overall the semiphenomenological densities computed here reproduce the interior fluctuations and surface geometries of the DME predictions remarkably well, especially when one considers that no attempt has been made to fit these DME distributions other than to obtain reasonable values of Δr_{np} by variation of R_n.

TABLE II. Single particle states in ^{40}Ca. All energies are in MeV and are relative to the ground state of ^{40}Ca. Experimental values are from Refs. 35–49.

Shell level	Pickup E_{B1}	Pickup S_1	Proton states $(p,2p)$ E_{B1}	Proton states $(e,e'p)$ E_{B1}	Particle $T_>$ E_{B3}	Particle $T_>$ S_3	E	V_L	$\langle\pi\rangle$	Neutron states E	Neutron states $\langle\nu\rangle$
$2p_{3/2}$	13.19	0.16			−0.70	3.76	−0.13	55.0	0.15	5.93	0.15
$1f_{7/2}$	2.82	0.58			1.08	7.36	1.21	50.3	0.56	8.93	0.56
$1d_{3/2}$	8.33	3.70	8.5 ± 2	10.9 ± 0.7	−1.02	0.32	7.59	52.7	3.59	15.63	3.59
$2s_{1/2}$	10.94	1.75	12 ± 1	14.4 ± 0.3			12 ± 1	57.4	1.70	18.19	1.70
$1d_{5/2}$	16 ± 1	6	16 ± 2	19.0 ± 1.1			19 ± 2	60.4	6	22.4	6
$1p_{1/2}$			31.5 ± 3.5	35 ± 1			31.5	66.7	2	26.6	2
$1p_{3/2}$			36 ± 3	35 ± 1			36 ± 3	68.3	4	46.48	4
$1s_{1/2}$			48.5 ± 5	59 ± 3			48.5	71.4	2	67.57	2

TABLE III. Single particle states in ^{48}Ca. All energies are in MeV and are relative to the ground state of ^{48}Ca. Experimental values are from Refs. 38, 41, 43, 46, 48, and 50–53.

Shell level	Proton states: Pickup E_{B1}	Pickup S_1	$(p,2p)$ E_{B1}	Particle $T_<$ E_{B2}	Particle $T_<$ S_2	Particle $T_>$ E_{B3}	Particle $T_>$ S_3	E	V_L	$\langle\pi\rangle$	Neutron states E	Neutron states $\langle\nu\rangle$
$2p_{3/2}$				6.08	3.96	−1.83	0.44	5.30	59.0	0.2	5.25	0.5
$1f_{7/2}$				9.62	8			9.62	57.8	0.3	10.11	7.5
$1d_{3/2}$	16.17	3.88						16.17	59.5	3.9	13.04	4
$2s_{1/2}$	16.45	1.79						16.45	59.4	1.6	13.08	2
$1d_{5/2}$	21.5 ± 1	4.34						23.5	62.1	6	21.96	6
$1p_{1/2}$			35 ± 10					35 ± 10	70.9	2	33.5	2
$1p_{3/2}$			35 ± 10					35 ± 10	72.6	4	37.8	4
$1s_{1/2}$			55 ± 10					55 ± 10	80.1	2	53.3	2

III. COMPUTATION OF THE PROTON-NUCLEUS ELASTIC SCATTERING CROSS SECTION

The technique used here to compute the proton-nucleus elastic scattering cross sections is the optical potential approach presented by Kerman, McManus, and Thaler (KMT).[12] The explicit form of the KMT optical potential to second order in the density is given in the appendix of Ref. 60, which makes use of the closure approximation. The explicit details which enable this second order optical potential to be numerically evaluated are given in Ref. 20 which discusses the impulse approximation and other simplifications needed to render the first and second order terms tractable. The necessary ingredients in these second order calculations are; (1) the free spin-dependent proton-nucleon scattering amplitudes, (2) the one-body proton and neutron point density distributions of the target nucleus ground state (computed in the previous section), and (3) target nucleon correlation functions. A complete discussion of the scattering formalisms and approximations used in analyzing proton-nucleus elastic scattering data near 1 GeV is given for example in Refs. 18, 20, and 21, and so will not be covered in detail here.

The full expression for the proton-nucleon scattering amplitude, $t(q)$, contains five independent terms.[61] For the even-even nuclei considered here the double spin-flip components of $t(q)$[61] do not contribute to the first order optical potential. Therefore, the full expression for $t(q)$ can be simplified to

$$t_{pj}(q^2) = t^0_{pj}(q^2) + it^s_{pj}(q^2)(\vec{\sigma}_p + \vec{\sigma}_j)\cdot\hat{n}\,, \tag{7}$$

where $\hat{n} = (\vec{k}_i \times \vec{k}_f)/|\vec{k}_i \times \vec{k}_f|$ and j refers either to target protons or neutrons. As is customary at energies near 1 GeV, these N-N amplitudes will be parametrized as[13–27]

$$\begin{aligned} t^0_{pj}(q^2) &= (ik_0\sigma^T_{pj}/4\pi)(1 - i\alpha_{pj})\exp(-B_{pj}q^2)\,, \\ t^s_{pj}(q^2) &= (ik_0\theta_{pj}/4\pi)(1 - i\alpha_{spj})(q^2/4M^2)^{1/2} \\ &\quad \times \exp(-B_{spj}q^2)\,, \end{aligned} \tag{8}$$

TABLE IV. Single particle states in ^{58}Ni. All energies, in MeV, are relative to the ground state of ^{58}Ni. The errors for the energies of the $1d_{3/2}$ and the deeper proton shells come from Ref. 40. The centroid of the $1d$ states is $E_d = 19.4 \pm 3.1$. Since ~20% uncertainties affect the measured spectroscopic factors, any value for the $2p_{3/2}$ occupation number between 0 and 1.5 is probably consistent with the data of the first line in the table. We assume that the $2s_{1/2}$ and the deeper shells are completely filled. Further experimental data are given in Refs. 40, 54, and 55.

Shell level	Proton states: Hole E_{B1}	Hole S_1	Particle $T_<$ E_{B2}	Particle $T_<$ S_2	Particle $T_>$ E_{B3}	Particle $T_>$ S_3	E	V_L	$\langle\pi\rangle$	Neutron states E	Neutron states $\langle\nu\rangle$
$2p_{3/2}$	9.84	0.25	2.56	2.42	−0.48	0.46	2.69	56.1	1.33	8.54	2
$1f_{7/2}$	8.72	7.37	1.79	0.66	−2.94	0.42	7.60	54.6	6.67	14.4	8
$2s_{1/2}$	11.16	1.31					11.16	53.3	2	17.56	2
$1d_{3/2}$	14 ± 2						14 ± 2	61.2	4	17.84	4
$1d_{5/2}$	23 ± 5						23 ± 5	61.2	6	22.6	6
$1p_{1/2}$	38 ± 5						38 ± 5	71.8	2	28.2	2
$1p_{3/2}$	42 ± 7						42 ± 7	71.8	4	30.7	4
$1s_{1/2}$	57 ± 7						57 ± 7	79.6	2	37.9	2

TABLE V. Single particle states in ^{64}Ni. All energies are in MeV and are relative to the ground state of ^{64}Ni. The experimental data used here are from Refs. 10 and 56.

Shell level	Proton states E	V_L	$\langle\pi\rangle$	Neutron states E	$\langle\nu\rangle$
$1f_{5/2}$				7.54	4
$2p_{3/2}$	2.69	54.4	0.25	9.57	4
$1f_{7/2}$	7.60	55.0	7.75	14.26	8
$1d_{3/2}$	14.0	56.7	4	22.96	4
$2s_{1/2}$	11.16	52.9	2	23.41	2
$1d_{5/2}$	23.0	62.6	6	30.8	6
$1p_{1/2}$	38.0	71.6	2	44.5	2
$1p_{3/2}$	42.0	73.8	4	48.7	4
$1s_{1/2}$	57.0	80.6	2	66.3	2

where k_0 is the nucleon momentum in the two nucleon center-of-momentum system and M is the nucleon mass. These two amplitudes give rise to the central and spin-orbit parts of the proton-nucleus optical potential as shown in Ref. 62. The values of the parameters of $t^0_{pj}(q^2)$ which reproduce N-N data at 800 MeV are given in Ref. 20. The present aggregate of N-N data at energies near 1 GeV is insufficient to enable a unique determination of the parameters of $t^s_{pj}(q^2)$ to be found so that these spin-dependent quantities must be determined by empirical fits to the proton-nucleus elastic analyzing power data, the values of which are given in Ref. 20 for the nuclei of interest here. These same spin-dependent parameters will be used in the calculations presented in the next section and good fits to the proton-nucleus analyzing power data are obtained.

TABLE VI. Single particle states in ^{116}Sn. All energies are in MeV and are relative to the ground state of ^{116}Sn. The experimental information used for this nucleus are from Refs. 10 and 57.

Shell level	Proton states E	V_L	$\langle\pi\rangle$	Neutron states E	$\langle\nu\rangle$
$2d_{3/2}$				8.92	1.31
$2d_{5/2}$				11.2	5.45
$1g_{7/2}$				10.3	5.96
$1g_{9/2}$	11.05	60.4	10	17.9	9.88
$2p_{1/2}$	11.79	60.6	2	20.9	1.98
$2p_{3/2}$	13.21	60.6	4	23.4	3.97
$1f_{5/2}$	14.26	60.6	6	24.0	5.96
$1f_{7/2}$	21.94	64.1	8	32.1	7.97
$2s_{1/2}$	27.2	66.9	2	39.6	2
$1d_{3/2}$	30.0	66.2	4	41.2	4
$1d_{5/2}$	35.2	70.9	6	46.2	6
$1p_{1/2}$	45.1	76.1	2	57.5	2
$1p_{3/2}$	47.6	77.4	4	59.8	4
$1s_{1/2}$	58.3	83.0	2	72.1	2

TABLE VII. Single particle states in ^{124}Sn. All energies are in MeV and are relative to the ground state of ^{124}Sn. The experimental data for ^{124}Sn are from Refs. 10 and 58.

Shell level	Proton states E	V_L	$\langle\pi\rangle$	Neutron states E	$\langle\nu\rangle$
$1h_{11/2}$				8.0	6.63
$2d_{3/2}$				8.58	2.87
$2d_{5/2}$				10.8	5.81
$1g_{7/2}$				9.97	7.18
$1g_{9/2}$	14.4	61.0	10	17.0	9.92
$2p_{1/2}$	15.1	61.6	2	19.7	1.99
$2p_{3/2}$	17.5	62.8	4	22.1	3.98
$1f_{5/2}$	19.8	64.1	6	22.7	5.97
$1f_{7/2}$	27.7	67.9	8	30.5	8
$2s_{1/2}$	33.1	71.2	2	37.5	2
$1d_{3/2}$	36.2	72.8	4	39.2	4
$1d_{5/2}$	41.0	75.2	6	44.0	6
$1p_{1/2}$	51.0	80.8	2	54.6	2
$1p_{3/2}$	53.4	81.9	4	56.8	4
$1s_{1/2}$	69.0	92.8	2	71.9	2

The specific form of the second order KMT optical potential used here is identical to that computed in Ref. 20 in which the second order term is proportional to a six dimensional integral over the coordinates of two target nucleons. This integral consists of the product of two nucleon-

TABLE VIII. Single particle states in ^{208}Pb. All energies are in MeV and are relative to the ground state of ^{208}Pb. The experimental data used for ^{208}Pb are from Refs. 10 and 59.

Shell level	Proton states E	V_L	$\langle\pi\rangle$	Neutron states E	$\langle\nu\rangle$
$3p_{1/2}$				7.38	2
$2f_{5/2}$				7.95	6
$3p_{3/2}$				8.27	4
$1i_{13/2}$				9.01	14
$1h_{9/2}$	3.77	61.3	0.25	10.85	10
$2f_{7/2}$	2.87	61.9	0.20	9.72	8
$3s_{1/2}$	8.03	62.6	1.55	18.5	2
$2d_{3/2}$	8.38	62.0	4	19.0	4
$1h_{11/2}$	9.37	60.6	12	19.6	12
$2d_{5/2}$	9.70	61.5	6	22.1	6
$1g_{7/2}$	11.43	61.3	8	23.3	8
$1g_{9/2}$	15.43	60.5	10	31.3	10
$2p_{1/2}$	20.0	66.6	2	33.3	2
$2p_{3/2}$	21.8	67.6	4	35.2	4
$1f_{5/2}$	26.1	69.7	6	37.3	6
$1f_{7/2}$	31.9	72.6	8	42.7	8
$2s_{1/2}$	34.1	72.1	2	48.3	2
$1d_{3/2}$	38.3	76.9	4	50.4	4
$1d_{5/2}$	41.7	76.9	6	53.5	6
$1p_{1/2}$	48.7	81.3	2	62.1	2
$1p_{3/2}$	50.3	82.0	4	63.4	4
$1s_{1/2}$	57.0	85.5	2	72.5	2

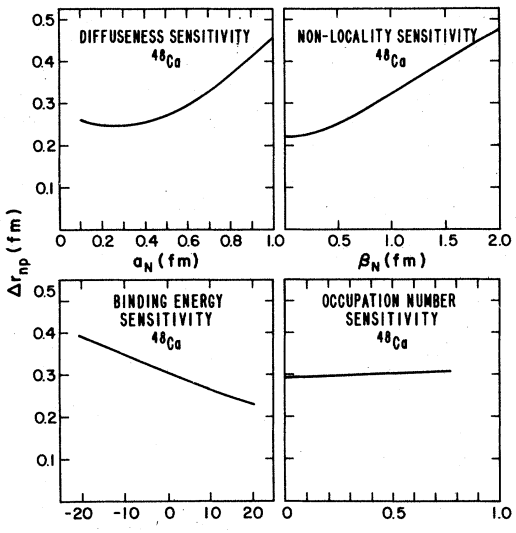

FIG. 1. Sensitivity of Δr_{np} ($\equiv \langle r_n^2 \rangle^{1/2} - \langle r_p^2 \rangle^{1/2}$) in ^{48}Ca to variations in (a) the neutron binding potential diffuseness, (b) the neutron nonlocality length, (c) the neutron binding energies, and (d) the neutron occupation number of the $2p_{3/2}$ single particle level.

nucleon t matrices and a two-body correlation function, $C_2(\vec{r}_1, \vec{r}_2)$. This two-body correlation function thus contains all of the complex nuclear dynamics inherent in the full two body nuclear wave function. Many studies[18,20,21,23,24] have determined that the most important nuclear correlations to be considered here are those due to the Pauli principle and to the short range nucleon-nucleon repulsive interaction. Following Boridy and Feshbach[24] $C_2(\vec{r}_1, \vec{r}_2)$ is thus approximated

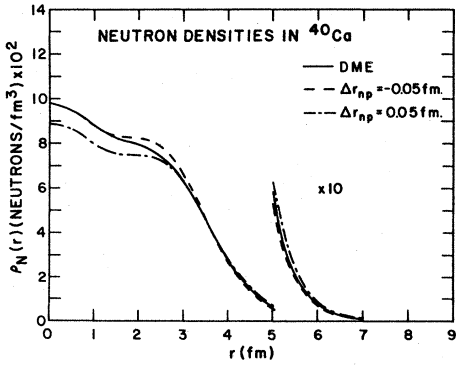

FIG. 2. Semiphenomenological point neutron density distributions in ^{40}Ca (dashed and dash-dot curves) compared with the predictions of the density matrix expansion code of Negele (Refs. 2,28) (solid curves). Note the two values of Δr_{np} assumed here. The densities in the tail region have been increased by a factor of 10 for clarity.

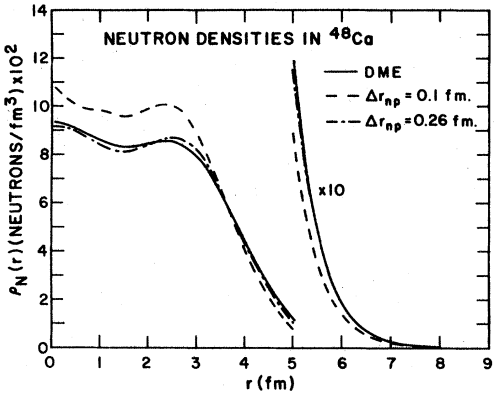

FIG. 3. Same as Fig. 2, except for ^{48}Ca.

by

$$C_2(\vec{r}_1, \vec{r}_2) \cong \rho(\vec{r}_1)\rho(\vec{r}_2)\{f_{\text{Pauli}}(|\vec{r}_1 - \vec{r}_2|) + f_{\text{SRD}}(|\vec{r}_1 - \vec{r}_2|) + f_{\text{Pauli}}(|\vec{r}_1 - \vec{r}_2|) f_{\text{SRD}}(|\vec{r}_1 - \vec{r}_2|)\}. \quad (9)$$

For a noninteracting Fermi gas the Pauli correlation function for a nucleus with A nucleons is[24]

$$f_{\text{Pauli}}(x) = -\tfrac{9}{4}[(A-4)/(A-1)][j_1(k_F x)/(k_F x)]^2, \quad (10)$$

where k_F is the local Fermi momentum, here assumed to be position dependent.[23] The short range dynamical (SRD) correlation is assumed to be[24]

$$f_{\text{SRD}}(x) = -\exp(-x^2/b^2) \quad (11)$$

with $b = 0.4$ fm.

By making the local density approximation and various short range and large nucleus assumptions as completely discussed in Ref. 20, local $\sim\rho^2$ expressions for the second order KMT optical potential are obtained. These second order terms are

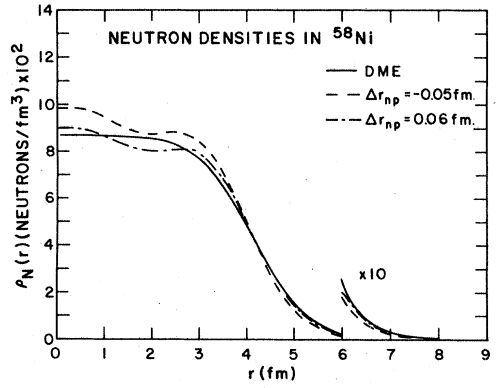

FIG. 4. Same as Fig. 2, except for ^{58}Ni.

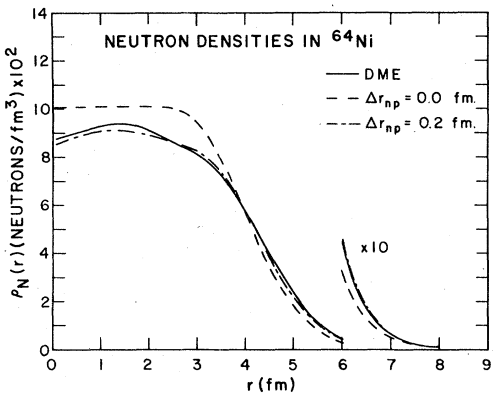

FIG. 5. Same as Fig. 2, except for ^{64}Ni.

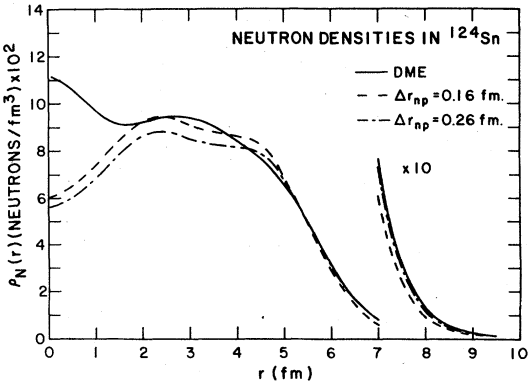

FIG. 7. Same as Fig. 2, except for ^{124}Sn.

proportional to $i\{t^0_{pj}(0)\}^2\rho^2(r)l_c$, where l_c is a length which is characteristic of the correlation range (i.e., k_F^{-1} or $b=0.4$ fm). The center-of-mass correlation correction has been estimated by the method of Chaumeaux, Layly, and Schaeffer.[21] Finally, the Pauli correlation correction to the spin-orbit part of the optical potential has been included here as given explicitly in Ref. 20. These $\sim\rho^2$ forms for the second order optical potential terms have been shown to be capable of adequately reproducing the less approximate coupled-channels calculations of Boridy and Feshbach[24] in which similar correlation effects are considered.

Thus the final, complete optical potential used in the calculations reported here is

$$U^{(1+2)\text{opt}}(r) = U^{(1)}(r) + U^{(2)\text{opt}}_{\text{Pauli}}(r) + U^{(2)\text{opt}}_{\text{SRD}}(r) + U^{(2)\text{opt}}_{\text{PSR-I}}(r) + U^{(2)\text{opt}}_{\text{c.m.}}(r) + U^{(2)\text{opt}}_{\text{Pauli,s.o.}}(r) + U_{\text{Coul}}(r), \quad (12)$$

where $U^{(1)}(r)$ is the usual first order, spin-dependent KMT optical potential given in detail in Ref. 63 and $U_{\text{Coul}}(r)$ is the Coulomb potential for for an extended nuclear charge density, $\rho_{\text{CH}}(r)$. The first three second order optical potential terms follow from the three terms of Eq. (9) and each second order term is given in detail in Ref. 20. The full potential, $U^{(1+2)\text{opt}}(r)$ is then inserted into the Schrödinger equation with relativistic kinematics[20,22] from which the proton-nucleus scattering amplitude is obtained.

Thus the point proton and neutron densities computed in Sec. II can be used to yield proton-nucleus elastic scattering cross sections. When analyzing polarized proton-nucleus elastic scattering data with Eq. (12) the proton densities are determined from empirical charge densities according to Bertozzi *et al.*[9] and Ref. 20, while the spin dependent N-N parameters of Eq. (8) and the point neutron density distributions are determined by simultaneous fits to the proton-nucleus cross section and analyzing power data.

Error analyses are given in Refs. 20 and 22 for the nuclei considered here and the densities computed in Sec. II will be compared to these uncertainty bands in the next section. It should be emphasized both here and below that the widths of these error envelopes correspond only to statistical and model dependent errors and do not include the very many systematic sources of un-

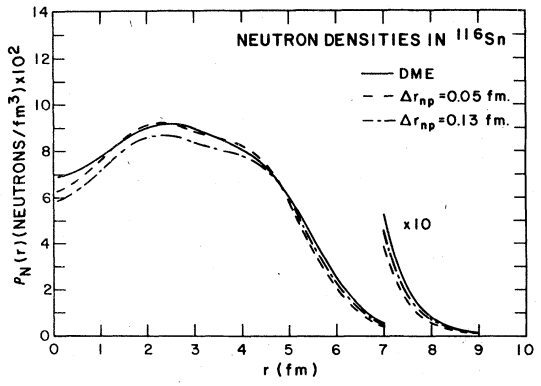

FIG. 6. Same as Fig. 2, except for ^{116}Sn.

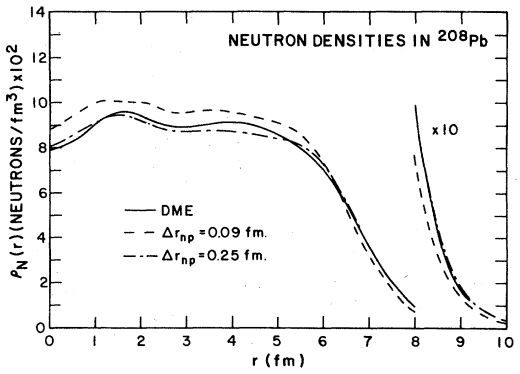

FIG. 8. Same as Fig. 2, except for ^{208}Pb.

certainty[22] which also affect the deduced neutron density distributions. The effects of these systematic errors have been given in Ref. 22 and if included in the error bands of Refs. 20, 22 and in Sec. IV below would broaden the total uncertainty envelopes in the nuclear surface region to about ± 0.003 neutrons/fm^3, typically, but would not greatly enlarge the already wide bands in the nuclear interior.

IV. COMPARISON OF THE COMPUTED AND THE "EMPIRICAL" NEUTRON DENSITIES

Using the methods of Sec. III, the proton-nucleus elastic scattering cross sections at 800 MeV which result from the proton and neutron point densities of Sec. II have been computed for ^{40,48}Ca, ^{58,64}Ni, ^{116,124}Sn, and ^{208}Pb. The angular distributions are shown in Figs. 9–11 along with the experimental data obtained with the high resolution spectrometer (HRS) at LAMPF.[13–16] The assumed values of Δr_{np} are shown for each nucleus in the appropriate figure where the cross sections which result from smaller neutron radii are shown as solid curves, while the calculations with the larger neutron radii are displayed by the dashed curves.

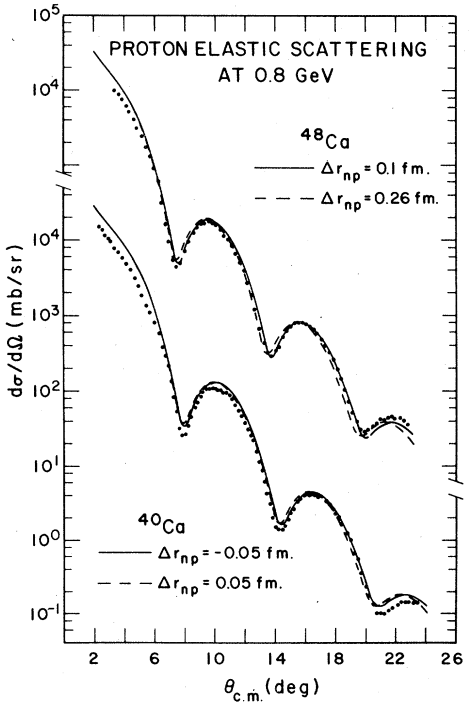

FIG. 9. Proton elastic scattering cross sections for ^{40,48}Ca at 800 MeV assuming the semiphenomenological proton and neutron densities computed here (solid and dashed curves). Note the two values of Δr_{np} assumed for each nucleus. The data are from Ref. 13.

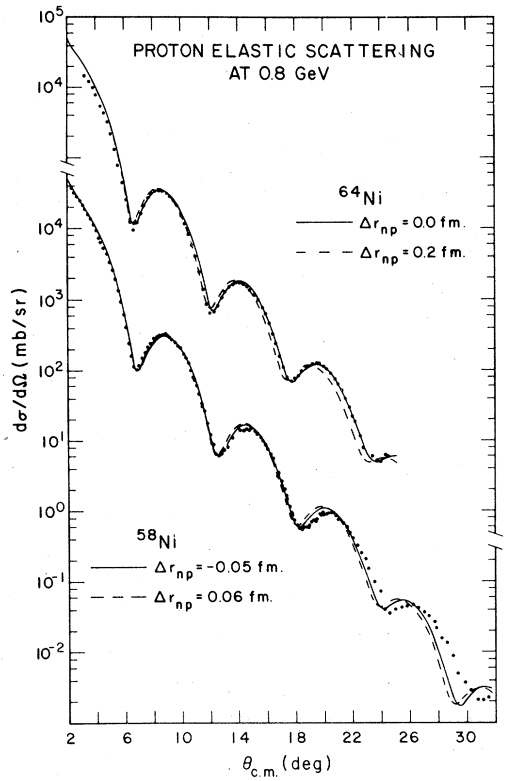

FIG. 10. Same as Fig. 9, except for ^{58,64}Ni. The data are from Ref. 14.

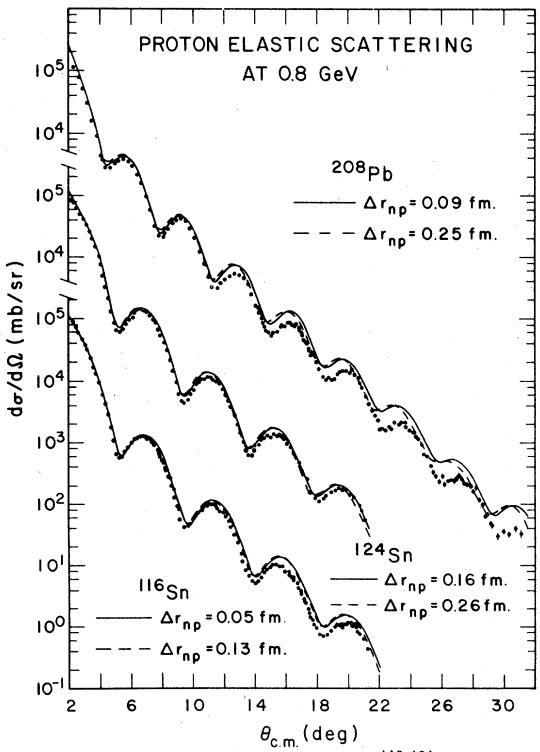

FIG. 11. Same as Fig. 9, except for ^{116,124}Sn and ^{208}Pb. The data are from Refs. 15 and 16.

The overall slopes of the diffractive patterns, the positions of the maxima and minima, and the general diffractive structure of the computed cross sections are seen in Figs. 9 and 10 to be in very good agreement with the calcium and nickel data. The failure of the calculated cross section to reproduce the forward angle ($\lesssim 7°_{c.m.}$) data of $p+{}^{40}$Ca has recently been attributed to experimental problems.[64] On the other hand, the failure of the computed angular distribution in the back angle region ($\gtrsim 20°_{c.m.}$) for ^{58}Ni is genuine, but similar discrepancies appear in empirical fits to this same data.[14] The significant result of these comparisons is that no serious deterioration in the fit quality occurs when the neutron number is increased by 8 and 6 in the calcium and nickel isotopes, respectively. One might naively expect that the neutron excess would alter the nuclear surface geometry in the neutron rich isotopes of calcium and nickel in such a way that a simple variation of the neutron binding potential radii could not account for. The results in Figs. 9 and 10 suggest that the method of Sec. II should be quite applicable to the calculation of neutron and matter densities in these medium weight nuclei from $A=40$ to 64.

The angular distributions for proton elastic scattering from ^{116,124}Sn and ^{208}Pb are shown in Fig. 11. Although the positions of the diffractive maxima and minima and the general shapes of the diffractive structure are in good agreement with the data, the overall slope of the diffractive pattern is too shallow in comparison with the data. By this it is meant that the ratios of successive maxima in the computed angular distributions are too small. Such a discrepancy is indicative of the smallness of the diffuseness of the computed matter density. From these three examples one can see that the calculational method of Sec. II predicts too small a value for the neutron surface thickness for neutron rich nuclei and indicates that both the neutron binding potential diffuseness as well as the potential radius should be freely varied when fitting matter densities in heavy nuclei with $A \gtrsim 100$.

The computed densities of Sec. II are compared with the empirically deduced neutron density envelopes of Refs. 20 and 22 in Figs. 12–15 as explained in the previous section. The reader should recall that these empirical error envelopes include statistical and model dependence uncertainties only. The densities computed by assuming the smaller values of Δr_{np} are indicated in Figs. 12–15 by the dashed curves, while those which correspond to the larger values of Δr_{np} are displayed by the dash-dot curves. The shaded regions indicate the empirically deduced results. The general, qualitative agreement is fairly good.

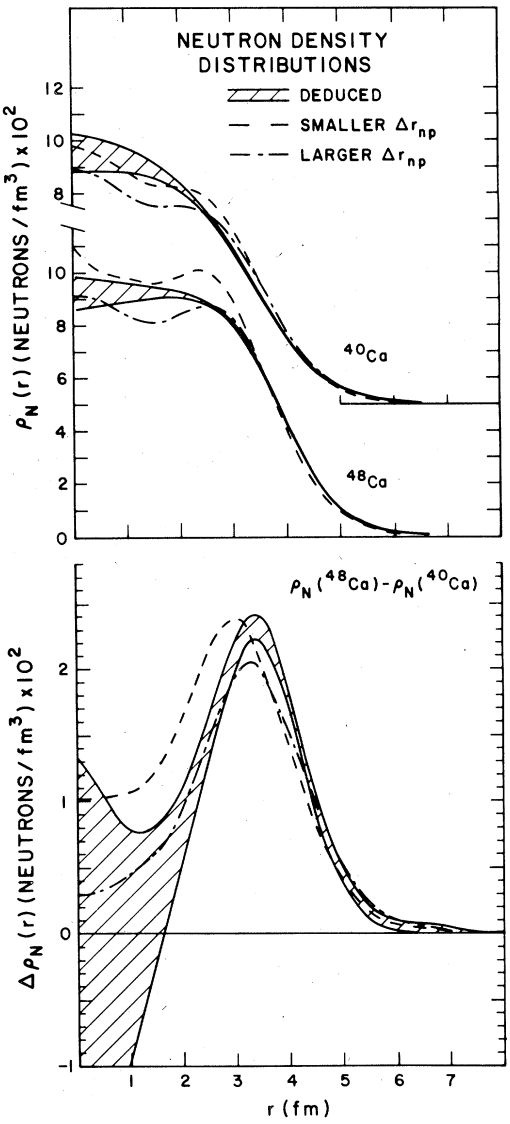

FIG. 12. Neutron density distributions for ^{40,48}Ca and the isotopic neutron density difference computed as described in the text. The shaded bands indicate the empirically deduced densities of Ref. 20, while the dashed and dash-dot curves represent the semiphenomenological results from Sec. II of the text in which the smaller and larger values of Δr_{np} given in the previous figures are assumed, respectively. Note the generally good agreement displayed in the lower half of the figure.

Notice that, as was the case with the angular distributions, no serious deterioration in agreement occurs when comparing the results for two isotopes as the neutron number is increased. Because of this the isotopic neutron density difference should be reliably computed by the techniques of Sec. II and Refs. 7 and 8, where a simple variation of the neutron binding potential radius alone should suffice.

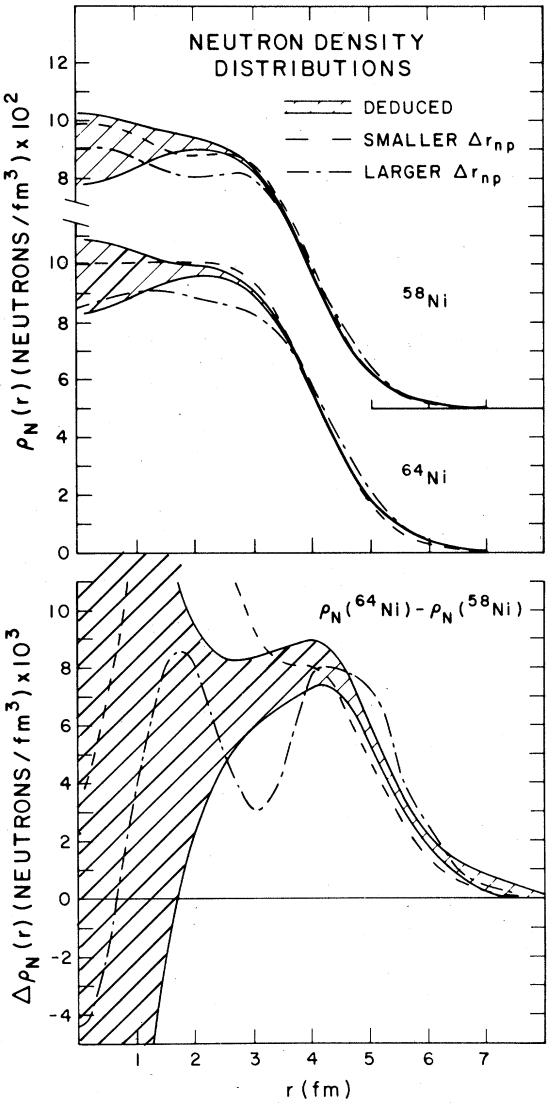

FIG. 13. Same as Fig. 12, except for ^{58,64}Ni.

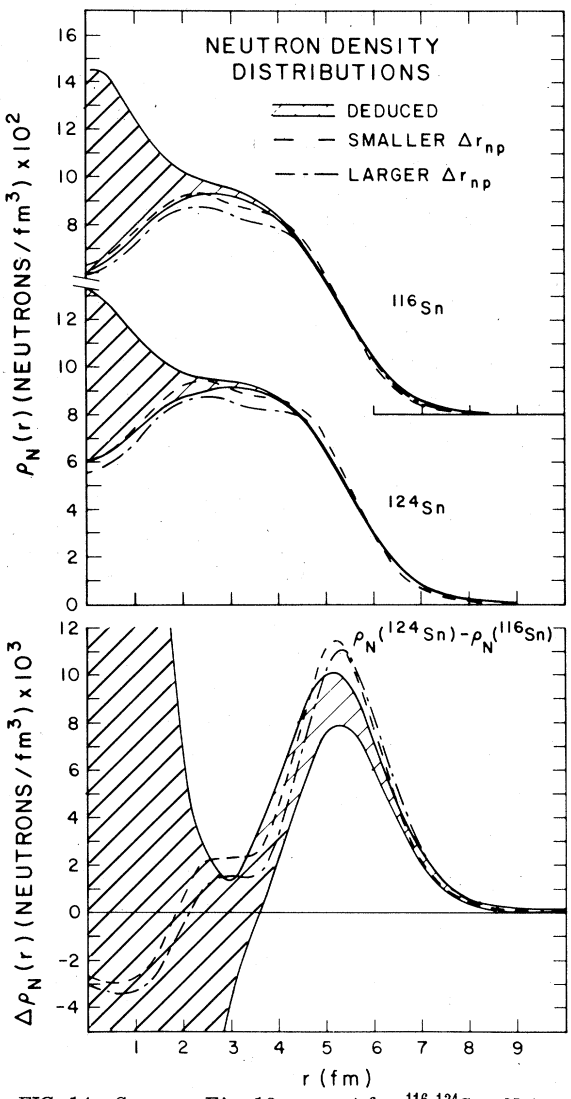

FIG. 14. Same as Fig. 12, except for ^{116,124}Sn. Note the qualitatively good agreement between the computed and the empirical isotopic neutron density difference in the lower part of the figure.

Probably the most reliable empirical information presently available for neutron densities are the isotopic differences.[20] Relative differences between the neutron densities of isotopes should be more accurately determined than the absolute densities themselves since most of the serious experimental and theoretical uncertainties cancel when computing the former.[20] Such empirical isotopic differences have been computed for ^{40,48}Ca, ^{58,64}Ni, and ^{116,124}Sn in Ref. 20 and the results are shown by the shaded bands in the lower halves of Figs. 12–14. The widths of the envelopes are due to statistical and model dependence errors and to the uncertainties in the empirical proton distributions for both isotopes.[20] The dashed (dash-dot) curves result from subtracting the computed neutron densities with the smaller (larger) Δr_{np} in the lighter isotopes from the den-

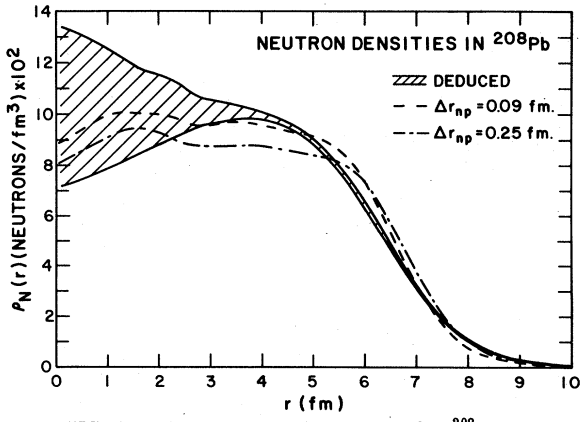

FIG. 15. Same as Fig. 12, except for ^{208}Pb.

sities with the smaller (larger) Δr_{np} in the heavier isotopes. The general agreement of the empirical bands with the theoretical curves in Figs. 12–14 is very good. The excess neutron surface "bump" is reproduced quite well by the calculations of Sec. II. The above discussion and the results in Figs. 12–14 suggest that in future work, one should test the compatibility of the single neutron transfer data with these empirically deduced neutron isotopic *differences* rather than the absolute densities themselves.

Finally, the moments of the computed neutron densities are compared with those of the DME predictions and the empirically deduced results. The kth moment of a spherically symmetric neutron density is defined to be

$$r^k \equiv \left(\frac{1}{N}\int_0^\infty \rho_n(r) r^k 4\pi r^2 dr\right)^{1/k}. \tag{13}$$

These moments have been computed for values of k from −2 to 6. The moments of the densities of Sec. II and the DME densities for each nuclei are shown in Figs. 16–22 relative to the mean values of the moments of the empirical densities. The solid curves indicate the DME result and the dashed (dash-dot) curves display the moments of the semiphenomenological densities in which the

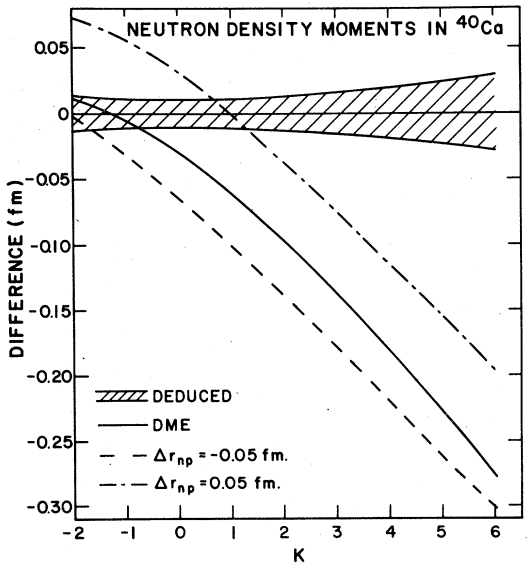

FIG. 16. Neutron density moments for ^{40}Ca as defined in Eq. (13) of the text. The moments of the densities of Sec. II of the text are indicated by the dashed and dash-dot curves, while the DME prediction is given by the solid line. The shaded band indicates the empirical result. The numerical values shown here correspond to differences between the moments of the theoretical densities and the mean value of the moments of the empirically deduced densities (see text).

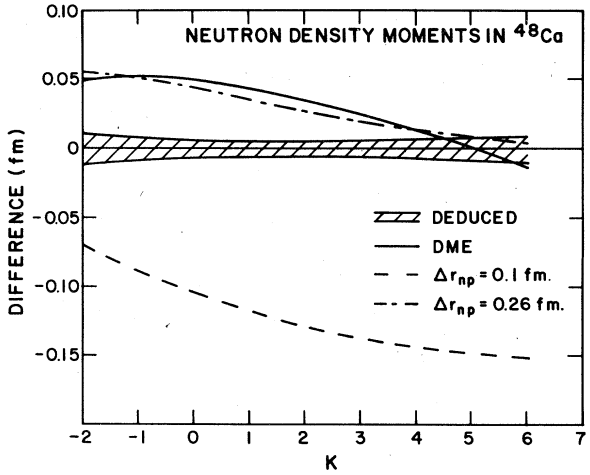

FIG. 17. Same as Fig. 16, except for ^{48}Ca.

smaller (larger) values of Δr_{np} are assumed. The total width of the shaded region in each figure indicates twice the uncertainty in the moments of the empirical densities due to statistical and model dependence errors only.

For each case in Figs. 16–22, except ^{124}Sn the moments of the densities of Sec. II display the same overall trend as do the DME density moments. Furthermore, it is seen that scaling the neutron binding potential radius shifts the value of each moment for $k = -2$ to 6 of the semiphenomenological densities by an approximately uniform amount. In fact one could fit the DME moment distribution in this range fairly well simply by adjusting the neutron binding potential radius. Carrying out such a fitting procedure should improve the comparisons shown in Figs. 2–8 somewhat. In comparison with the moments of the empirical densities the theoretical densities tend

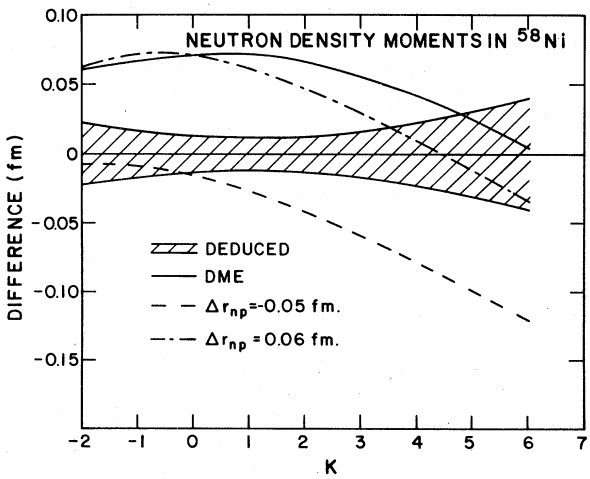

FIG. 18. Same as Fig. 16, except for ^{58}Ni.

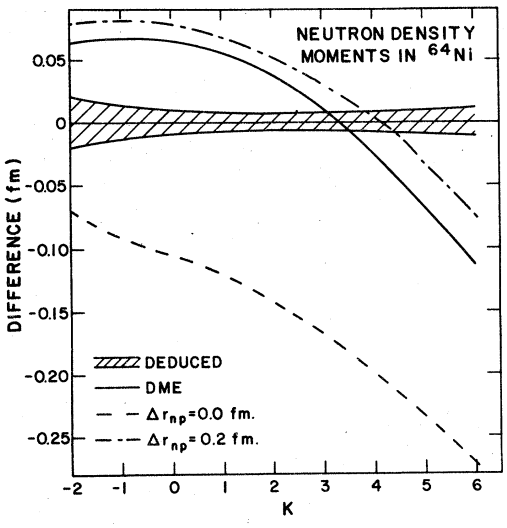

FIG. 19. Same as Fig. 16, except for ^{64}Ni.

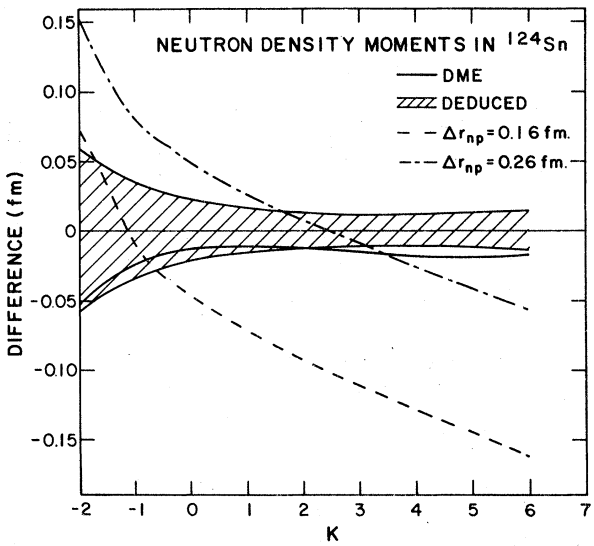

FIG. 21. Same as Fig. 16, except for ^{124}Sn.

to have larger values for the lower moments, while the higher moments are somewhat too small. This tendency can be understood directly from the radial distributions by observing in Figs. 12–15 that in the tail region, the theoretical densities are depleted in relation to the empirically deduced distributions. Notice of course that these differences in moments are only of the order of 0.1 to 0.2 fm with respect to the moments themselves which vary from about 3 to 6 fm.

For the case of ^{124}Sn a DME calculation in which no filling of the $3s_{1/2}$ single particle level is assumed produces a neutron density moment dependence similar in shape to those of the semiphenomenological densities indicated by the dashed and dash-dot curves in Fig. 21. This new DME neutron density has an rms radius which is 0.015 fm smaller than the empirical value. This sensitive behavior of the density moment decomposition to the details of the occupation probabilities of the last few single particle levels indicates the value of this particular method of comparing various theoretical and experimental densities.

V. CONCLUSIONS

In this work the semiphenomenological method of Refs. 7 and 8 for computing nuclear charge densities has utilized experimental binding energy and spectroscopic information obtained from

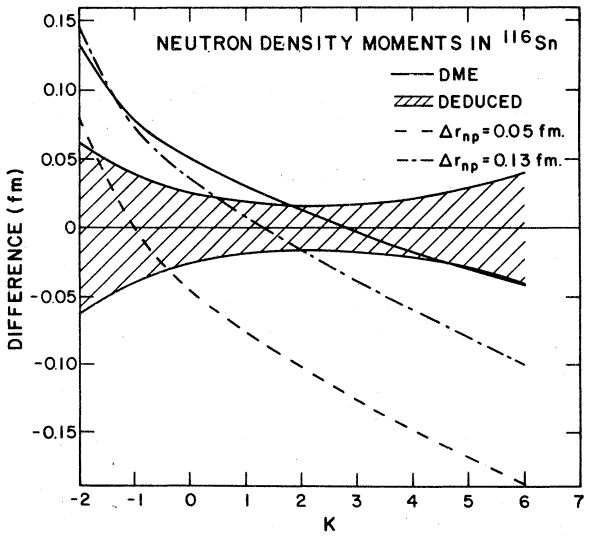

FIG. 20. Same as Fig. 16, except for ^{116}Sn.

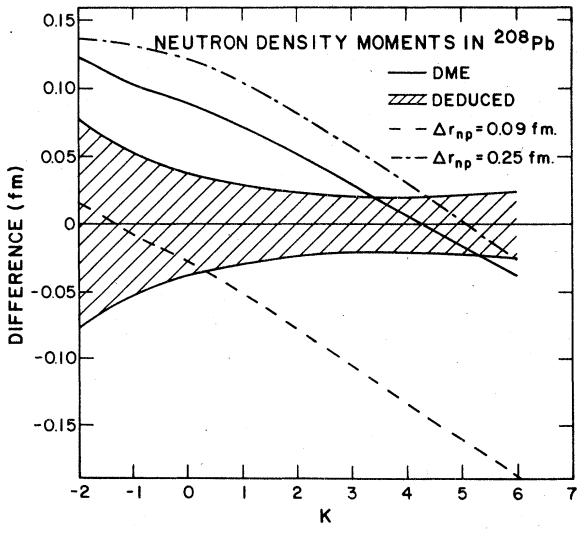

FIG. 22. Same as Fig. 16, except for ^{208}Pb.

single neutron transfer reactions to extend the previous calculations to include both the proton and neutron one body densities. These are generated by summing the squares of single particle wave functions with proper attention being given to nonorthogonality problems and center-of-mass corrections. This method of phenomenologically relating the single proton transfer data to the high quality empirical charge distributions of nuclei, as determined by electron scattering and muonic atom data, has proven to be quite successful for ^{16}O, ^{39}K, ^{40,48}Ca, ^{58}Ni, ^{90}Zr, and ^{208}Pb.[7,8,10]

These same techniques have been used to generate neutron distributions for a number of nuclei which have been studied with the recently developed 800 MeV polarized proton beam at LAMPF.[13-16] These theoretical neutron densities have been compared to those empirically deduced from second order KMT analyses[20] of these new high quality proton data. In general the resulting proton-nucleus cross sections and the neutron density distributions and moments are in good agreement with the eleastic scattering data and with both the empirically deduced densities and those of the density matrix expansion formalism.[2,28] It has also been shown that the isotopic neutron density differences computed in Sec. II and as deduced from proton-nucleus data are in very good agreement with one another. This particular test of the applicability of these semiphenomenological densities is significant since isotopic differences are believed to be the most reliably determined quantity obtained from analyses of proton-nucleus elastic scattering at present.[20] From Figs. 12–14 one sees that these differences are indeed well defined by the above theoretical predictions. In future studies the semiphenomenological approach of Sec. II would be best applied to relating the single neutron transfer data to these isotopic neutron differences.

Systematic discrepancies between the semiphenomenological densities and the empirically deduced distributions do occur, however. For ^{116,124}Sn and ^{208}Pb one observes in Fig. 11 that the diffuseness of the computed densities should be increased in order to better describe the cross section data. In Figs. 16–22 the neutron density moments are seen to be in slight disagreement with the empirical results (of the order of 0.1 to 0.2 fm), the computed density moments tending to decrease with increasing k relative to the empirical values.

In Figs. 2–8 and 16–22 we see that these semiphenomenological densities qualitatively reproduce the interior shapes, the surface geometries, and the density moments of the density matrix expansion variant of Hartree-Fock theory. Sensitivity to the occupation probability of the $3s_{1/2}$ single particle level in ^{124}Sn demonstrates the importance of configuration mixing in these single particle levels near the Fermi surface. The usefulness of density moment decompositions in studying such effects is also demonstrated here, and this method is also seen to be a valuable means for comparing various theoretical densities.

The success demonstrated here in this initial attempt to connect the tremendous knowledge of nuclear structure gained through many single nucleon transfer reaction studies to nuclear matter density information recently gained from intermediate energy proton elastic scattering analyses is very encouraging. Clearly, a semiphenomenological fitting calculation which tests the compatability of the single neutron transfer data and the empirically deduced neutron densities should prove to be as rewarding as the earlier calculations of nuclear charge densities, especially if applied to isotopic neutron differences. The usefulness of such a model in fitting proton-nucleus elastic scattering data becomes immediately apparent since the density model of Refs. 7 and 8 is much more physically grounded than other models which are generally used, such as the Fermi or Gaussian models.[22]

ACKNOWLEDGMENTS

We thank Mrs. S. Trumper for assistance with the calculations of the matter densities, which were made using a computer program developed in collaboration with Dr. F. Malaguti, Dr. A. Uguzzoni, and Dr. E. Verondini. This research was supported in part by the United States Department of Energy.

[1]J. W. Negele, Phys. Rev. C 1, 1260 (1970).
[2]J. W. Negele and D. Vautherin, Phys. Rev. C 5, 1472 (1972).
[3]X. Campi and D. W. Sprung, Nucl. Phys. A194, 401 (1972).
[4]L. R. B. Elton, Phys. Rev. 158, 970 (1967).
[5]C. J. Batty and G. W. Greenlees, Nucl. Phys. A133, 673 (1969).
[6]K. T. R. Davies and R. J. McCarthy, Phys. Rev. C 4, 81 (1971); and K. T. R. Davies, R. J. McCarthy, and P. U. Sauer, *ibid.* 7, 943 (1973).
[7]F. Malaguti, A. Uguzzoni, E. Verondini, and P. E.

Hodgson, Nucl. Phys. A297, 287 (1978).
[8]F. Malaguti, A. Uguzzoni, E. Verondini, and P. E. Hodgson, Nuovo Cimento 49A, 412 (1979).
[9]W. Bertozzi, J. Friar, J. Heisenberg, and J. W. Negele, Phys. Lett. 41B, 408 (1972).
[10]K. Bear and P. E. Hodgson, J. Phys. G 4, L287 (1978).
[11]R. J. Glauber, in *Lectures in Theoretical Physics*, edited by W. E. Brittin and L. G. Dunham (Interscience, New York, 1959), p. 315; see also *High Energy Physics and Nuclear Structure*, edited by G. Alexander (North-Holland, Amsterdam, 1967), p. 311; and *High Energy Physics and Nuclear Structure*, edited by S. Devons (Plenum, New York, 1970), p. 207.
[12]A. K. Kerman, H. McManus, and R. M. Thaler, Ann. Phys. (N.Y.) 8, 551 (1959).
[13]G. Igo *et al.*, Phys. Lett. 81B, 151 (1979).
[14]G. W. Hoffmann *et al.*, Phys. Lett. 79B, 376 (1978).
[15]G. W. Hoffmann *et al.*, Phys. Lett. 76B, 383 (1978).
[16]G. W. Hoffmann *et al.*, Phys. Rev. Lett. 40, 1256 (1978).
[17]G. Bruge, internal report, Saclay, DPh-N/ME/78-1, 1978 (unpublished).
[18]G. D. Alkhazov, S. L. Belostotsky, and A. A. Vorobyov, Phys. Rep. 42C, 89 (1978), and references therein.
[19]G. D. Alkhazov *et al.*, Phys. Lett. 57B, 47 (1975); Report No. LINP-244, Leningrad, 1976 (unpublished).
[20]L. Ray, Phys. Rev. C 19, 1855 (1979).
[21]A. Chaumeaux, V. Layly, and R. Schaeffer, Ann. Phys. (N.Y.) 116, 247 (1978).
[22]L. Ray, W. R. Coker, and G. W. Hoffmann, Phys. Rev. C 18, 2641 (1978).
[23]D. R. Harrington and G. K. Varma, Nucl. Phys. A306, 477 (1978).
[24]E Boridy and H. Feshbach, Ann. Phys. (N.Y) 109, 468 (1977).
[25]S. J. Wallace, Phys. Rev. C 12, 179 (1975); and B. Mulligan, Ann. Phys. (N.Y.) 26, 159 (1964).
[26]I. Brissaud and M. K. Brussel, Phys. Rev. C 15, 452 (1977).
[27]L. Ray, Phys. Rev. C 20, 1857 (1979).
[28]The DME code of J. W. Negele provided all of the numerical results given here.
[29]F. G. Perey, in *Direct Interactions and Nuclear Reaction Mechanisms*, edited by E. Clemental and C. Villi (Gordon and Breach, New York, 1963), p. 125.
[30]H. Fiedeldey, Nucl. Phys. 77, 149 (1966).
[31]I. Sick, Phys. Lett. 53B, 15 (1974), and private communication.
[32]I. Sick *et al.*, Phys. Rev. Lett. 35, 910 (1975).
[33]B. Frois *et al.*, Phys. Rev. Lett. 38, 152 (1977).
[34]C. W. de Jager, H. de Vries, and C. de Vries, At. Data Nucl. Data Tables 14, 479 (1974).
[35]R. Bock, H. H. Duhm, and R. Stock, Phys. Lett. 18, 61 (1965).
[36]J. C. Hiebert, E. Newman, and R. H. Bassel, Phys. Rev. 154, 898 (1967).
[37]R. Santo, R. Stock, J. H. Bjerregaard, Ole Hansen, O. Nathan, R. Chapman, and S. Hinds, Nucl. Phys. A118, 409 (1968).
[38]A. N. James, P. T. Andrews, P. Kirkby, and B. G. Lowe, Nucl. Phys. A138, 145 (1969).
[39]D. H. Youngblood, R. L. Kozub, R. A. Kenefick, and J. C. Hiebert, Phys. Rev. C 2, 477 (1970).
[40]R. L. Becker, Phys. Lett. 32B, 263 (1970).
[41]P. Doll, G. J. Wagner, K. T. Knöpfle, and G. Mairle, Nucl. Phys. A263, 210 (1976).
[42]K. Nakamura, S. Hiramatsu, T. Kamae, H. Muramatsu, and N. Izutsu, and Y. Watase, Nucl. Phys. A271, 221 (1976).
[43]P. Doll and G. J. Wagner, in Proceedings of the International Conference on the Physics of Medium-Light Nuclei, Florence, 1977, p. 88.
[44]T. A. Belote, A. Sperduto, and W. W. Buechner, Phys. Rev. 139, B80 (1965).
[45]T. A. Belote, W. E. Dorenbusch, and J. Rapaport, Nucl. Phys. A120, 401 (1968).
[46]J. Rapaport, W. E. Dorenbusch, and T. A. Belote, Nucl. Phys. A177, 307 (1971).
[47]G. Hauser, R. Löhken, G. Nowicki, H. Rebel, G. Schatz, G. Schweimer, and J. Specht, Nucl. Phys. A182, 1 (1972).
[48]P. Martin, M. Buenerd, Y. Dupont, and M. Chabre, Nucl. Phys. A185, 465 (1972).
[49]J. Källne, Uppsala University Report No. GWI-PH 2/74, 1974 (unpublished).
[50]J. R. Erskine, A. Marinov, and J. P. Schiffer, Phys. Rev. 142, 633 (1966).
[51]G. Sartoris and L. Zamick, Phys. Rev. 167, 1035 (1968).
[52]E. Kashy, A. Sperduto, H. A. Enge, and W. W. Buechner, Phys. Rev. 135, B865 (1964).
[53]J.L. Yntema, Phys. Rev. 186, 1144 (1969).
[54]J. Rapaport, Nucl. Data Sheets B3, 103 (1969); and A. G. Blair and D. D. Armstrong, Phys. Rev. 151, 930 (1966).
[55]H. J. Kim, Nucl. Data Sheets 17, 485 (1976); J. Bommer, H. Fuchs, K. Grabisch, H. Kluge, W. Ribbe, and G. Röschert, Nucl. Phys. A199, 115 (1973); and D. J. Pullen and B. Rosner, Phys. Rev. 170, 1034 (1968).
[56]R. L. Auble, Nucl. Data Sheets 14, 119 (1975); 16, 351 (1975).
[57]S. Raman and H. J. Kim, Nucl. Data Sheets 16, 195 (1975); and R. L. Auble, *ibid.* 25, 315 (1978).
[58]R. L. Auble, Nucl. Data Sheets B7, 363 (1972); B7, 465 (1972).
[59]M. R. Schmorak, Nucl. Data Sheets 22, 487 (1977); and M. J. Martin, *ibid.* 22, 545 (1977).
[60]H. Feshbach, A. Gal, and J. Hüfner, Ann. Phys. (N.Y.) 66, 20 (1971).
[61]M. J. Moravcsik, *The Two-Nucleon Interaction* (Clarendon, Oxford, 1963), pp. 11–18.
[62]E. Lambert and H. Feshbach, Ann. Phys. (N.Y.) 76, 80 (1973).
[63]E. Kujawski and J. P. Vary, Phys. Rev. C 12, 1271 (1975).
[64]G. W. Hoffmann and G. Igo, private communication.